Published in final edited form as:
Phys Med Biol. 2010 January 7; 55(1): 265–280. doi:10.1088/0031-9155/55/1/016.

Studies of the interactions of an MRI system with the shielding in a combined PET/MRI scanner

Bo J. Peng[1], **Jeffrey H. Walton**[2], **Simon R. Cherry**[1], and **Jacob Willig-Onwuachi**[3]

[1]Department of Biomedical Engineering, University of California, Davis, Davis, CA, United States

[2]NMR Facility, University of California, Davis, Davis, CA, United States

[3]Department of Physics, Grinnell College, Grinnell, IA, United States

Abstract

A positron emission tomography (PET) system or 'insert' has been constructed for placement and operation in the bore of a small animal magnetic resonance imaging (MRI) scanner to allow simultaneous MR and PET imaging. The insert contains electronics, components with a variety of magnetic properties, and large continuous sheets of metal— all characteristics of an object that should, by conventional wisdom, never be placed in the bore of an MR scanner, especially near the imaging volume. There are a variety of ways the two systems might be expected to interact that could negatively impact the performance of either or both. In this article, the interaction mechanisms, particularly the impacts of the PET insert and shielding on MR imaging, are defined and explored. Additionally, some of the difficulties in quantifying errors introduced into the MR images as a result of the presence of the PET components are demonstrated. Several different approaches are used to characterize image artifacts and determine optimal placement of the shielding. Data are also presented that suggest ways the shielding could be modified to reduce errors and enable placement closer to the isocenter of the magnet.

1. Introduction and Background

1.1. Motivation

Recently, the benefits of multimodality imaging have received a great deal of attention (Zaidi *et al*., 2007; Gaa *et al*., 2004; Jacobs and Cherry, 2001; Townsend, 2008). In particular, dual imaging modalities that offer anatomical and functional information have become immensely useful in both research and clinical applications. This article focuses on development work for the particular combination of positron emission tomography (PET) and magnetic resonance imaging (MRI). If combined so as to generate co-registered images, PET—with an appropriate tracer agent—can be used to identify and study a particular molecular target or pathway, while MRI can be used to identify exactly where this process is taking place and to characterize the participating or surrounding tissue. Combining these modalities for simultaneous or co-aligned imaging offers significantly more information than either modality alone or even than combined but not simultaneous or co-aligned MRI and PET studies.

Another modality commonly used in combination with PET is computed tomography (CT). MRI offers a number of advantages over CT that make it a good candidate for combination with PET. First, although CT can provide better spatial resolution, MRI has much better soft tissue contrast (a result of the range of tissue properties that can be used as endogenous contrast

jlvpeng@ucdavis.edu.

mechanisms, including the relaxation times, diffusion, perfusion, flow velocity, temperature, elasticity, oxygenation level, susceptibility, magnetization transfer, temperature, and more), which enables significantly improved differentiation and determination of tissue composition (Tidwell and Jones, 1999) even for tissues of similar density. MRI also eliminates the additional ionizing radiation from CT. Moreover, MR can improve the resolution of the PET images because the strong magnetic field limits the positron range prior to annihilation (Christensen *et al.*, 1995). Certainly MRI has drawbacks, including longer imaging times; larger physical gantry size; gradient coil noise; metal implant safety concerns; high manufacturing and maintenance costs, and increased difficulty implementing attenuation correction of the PET data (which can be accomplished using MR images (Zaidi *et al.*, 2007)) compared to PET/CT. However, the potential advantages of MRI for this application were encouraging enough to inspire the construction of prototype PET/MRI systems (Judenhofer *et al.*, 2008; Catana *et al.*, 2008; Shao *et al.*, 1997).

1.2. Mechanisms of Interaction

There are many challenges in constructing a combined PET/MRI scanner. Interference between the PET and MRI subsystems can negatively impact the performance of both modalities. In this section we outline the primary interaction mechanisms: first summarizing how the MR scanner's high-magnetic-field environment impacts the design and operation of the PET system and then discussing in a bit more detail how the presence of the PET system can impact the performance of the MRI. The mechanisms discussed are not newly discovered principles, but in light of recent research on PET detectors in the MR scanner bore, we feel it is important to revisit them all briefly in this context as a consolidated reference and resource for this and future work. For descriptions of MR compatibility issues for other devices and other contexts see, for example (Chinzei *et al.*, 1999; Chinzei and Miller, 2001; Tse *et al.*, 2009).

First, the MR scanner's magnetic field affects the choice or use of the PET light collection device. Typically, PET scanners are built using photomultiplier tubes (PMTs), which are sensitive to magnetic fields and are generally unable to operate properly in the presence of a strong magnetic field such as is present in or near the bore of an MR magnet. It is possible to use long fiber optic cables to couple the PET scintillator crystals to the PMTs at a remote location where the magnetic field is weaker (Slates *et al.*, 1999; Shao *et al.*, 1997). However, the long fiber optic cables degrade the performance of the PET system. Two more recent PET designs (Catana *et al.*, 2008; Judenhofer *et al.*, 2008) use an alternate light collection device (a semiconductor detector) called an avalanche photodiode (APD) that is capable of operating in a magnetic field (Lewellen, 2008). This enables placement of entire detectors in the bore of the MR scanner and therefore necessitates a careful examination of all potential interactions between the MRI and PET systems.

Alternatively, the MRI system can be redesigned around a more traditional PET system with PMTs, for example with a split coil (Lucas *et al.*, 2006) or a field-cycled MRI system (Gilbert *et al.*, 2006). Though the relevant data has not yet been published regarding the performance of these combined systems, the expensive costs of redesigning the MRI system and the relatively low main magnetic field that each uses could be problematic for these designs.

Another mechanism of interaction is radiofrequency (RF) crosstalk between the PET and MRI electronics. Consequently, in a combined PET/MR system, shielding is introduced to minimize RF interaction. The RF signals detected in MRI are small in amplitude and achieving reasonable signal-to-noise ratio (SNR) requires careful attention to the RF environment the scanner is in. Bringing any electronics into the scan room, especially into the bore, can significantly interfere with MR signal detection. The PET electronics are also fairly sensitive and one could imagine that the sometimes-powerful RF transmission in MRI might have a detrimental impact on the PET acquisition.

Ironically, however, the introduction of shielding intended to reduce RF interactions discussed above has the potential to introduce alternate negative interactive effects. For example, the RF coils in the MR scanner are designed to couple to the biological sample in a particular way. If there is other metal nearby the intended coupling to the sample can be altered.

Perhaps the most significant concerns with the physical presence of the shielding, however, are related to the uniformity of the magnetic fields used by the MR scanner. The shielding metal (as well as some of the other structures and electronics of the PET insert) has the potential to interact with the main magnetic field (B_0) or the gradients in ways that degrade the uniformity of B_0 and the overall performance of the MRI scanner. First, the shielding is certain to have magnetic susceptibility different from the surrounding air. The interfaces between volumes of differing susceptibility cause local magnetic field variations that disturb the uniformity of B_0. In addition, the switching of the gradient field coils causes time-varying magnetic fields that can induce eddy currents on the shielding via Faraday induction. These eddy currents in turn cause local magnetic fields that decrease the B_0 uniformity. Lastly, if the gradient coils couple to the shielding and generate eddy currents, then the ability to turn the gradient fields on and off in a controlled way is compromised, impacting the spatial encoding and speed of the MRI.

In short, placing the electronics and metal associated with the PET insert into the bore of an MR scanner seems at first like a challenging proposition because of all the potential negative impacts, particularly on the MR imaging. To summarize, expected mechanisms of potential interaction between the PET and MR systems include: 1) eddy current artifacts, 2) degradation of gradient coil performance, 3) RF noise or signal loss, and 4) susceptibility artifacts or other non-uniformities in the main magnetic field. Each of these interactions is addressed and explored in this article to varying degrees.

Our primary focus in this work is studying the effect of the PET/MR shielding on MR imaging because the shielding is the closest structure to the MR imaging volume and is expected to be a main cause of all four of the above listed interactions. We use a number of different simplified models of the PET/MR shielding (as well as the full prototype insert itself) in order to study the mechanisms of interaction with the MR system. Note that since much of our discussion and data involve these simplified shield models (cylindrical copper structures), our results may be relevant to other objects and devices to be placed in an MR scanner.

2. Design and Testing Considerations

2.1. Shielding materials

The shielding for the PET insert and the shielding models tested were all made of copper. The required thickness of the shielding material is determined primarily by the frequency range of the RF noise to be excluded. The amplitude of an electromagnetic (EM) wave incident on a conductive medium decays exponentially with depth into the conductor. The skin depth or e-folding length describing this decay (Ulaby, 2001; Shen and Kong, 1995) depends on the frequency of the wave and on the resistivity and permeability of the material. Our primary concern is noise close to the 300 MHz operating frequency of the MR scanner used in this work. Our calculations indicate that radiation at 300 MHz is attenuated 99% by a copper thickness of 18.9 μm (note that this number is only given as a reference point, and that 99% attenuation may not provide adequate shielding for all sources). Lower frequencies require thicker shielding for the same level of attenuation. For comparison, shielding of 10 MHz EM waves requires approximately 0.1 mm of copper, though it is not clear that frequencies this low need to be shielded for our system. Note also that most clinical scanners today operate at 64 or 128 MHz (1.5 or 3 T, respectively), and may require thicker shields.

Temperature also affects the skin depth of a conductor. The PET electronics are cooled by circulated nitrogen gas, so we also simulated anticipated variation in required shielding thickness with temperature (Giancoli, 1995). However, our simulations indicated that effective shielding depth does not vary significantly over the temperature range of interest when the frequency is above 1 MHz. Temperature effects are more significant for frequencies in the kilohertz range. Our simulations indicated, for example, the skin depth of copper for 10 kHz RF waves changed by 1.06×10^{-4} m for each 10 degrees C variation in temperature compared to 6.10×10^{-7}m per 10 degrees C for 300 MHz RF.

2.2. Baseline system variation

It is nearly impossible to prevent small drifts or variations in system performance over time. However these changes—or rather the effects of these changes on our measurements—can be characterized and quantified for consideration in the interpretation of the results of our experiments. RF noise, field strength, sample properties, and other MR system characteristics can vary with temperature and time. Additionally, tuning and shimming the MR system causes changes in data collection. This is a serious concern for our study because we have to move objects in the bore, requiring us to retune and reshim (just as one does prior to imaging different anatomical regions in a subject) and leading to this additional inherent source of variation. Note that even without moving the object or shield, the computer macros for tuning and shimming may determine slightly different settings each time they are run simply as a result of multiple local solutions to the minimization problem involved or slightly different initial settings and conditions.

2.3. Shielding placement

In order to determine how the presence of the shielding or PET insert affects MRI acquisition, artifacts or errors must be quantified. One straightforward technique for quantifying the amount of MRI error resulting from the presence of the shielding is to compare an image with the shielding in place to a reference image taken without the shielding. Unfortunately, because the images in this study are acquired at different times and the shielding has to be moved between acquisitions, this technique is susceptible to two undesired errors: temporal variation in system performance and motion of the sample between scans (the RF coil is inside the radius of the insert, making it a challenge to move the shielding without moving the sample being imaged).

Our goal was to determine how far away the PET electronics system and shielding should be located from the magnet isocenter to minimize interference between the two systems and optimize performance. From the perspective of the MRI system, it is always better to place any electronics or metal objects as far as possible away from the isocenter. However, from the perspective of the PET system, an increased distance from isocenter (where the scintillator crystals are) means an increased path length for and reduced efficiency of the transfer of scintillation light via the optical fibers to the APDs and consequently reduced SNR for each detected PET event. Therefore, careful investigation of the placement of the shielding is warranted to build a system that performs well during simultaneous MRI and PET imaging.

2.4. Chemical shift imaging—an alternate way to characterize image errors

As was mentioned above, there are a number of challenges and problems associated with the method of quantifying image errors by comparison with a reference image acquired at a separate time. In order to be more confident about the presence or absence of eddy current induced error or other artifacts, we developed a new technique to analyze the effects of the shielding using chemical shift imaging (CSI) (for a review see Rumpel and Pope, 1993 and references therein). This technique also requires a separately acquired reference data set, however, these reference data can be acquired immediately before or after the data set it will be compared to. Also, nothing needs to be physically moved between acquisition of the test

and reference data sets and consequently the same acquisition and shim settings are used for both.

CSI is often used to study chemical components of the tissue of interest by providing spectra of the signal. CSI can also be used, however, to examine the shifting of a single peak resulting from variations in the local magnetic field. With a slight modification, CSI can also be used to study eddy current fields in a controlled way. We inserted a strong gradient pre-pulse prior to CSI data acquisition to purposely induce eddy currents on the shielding or PET insert for quantification and study. Although the gradient switching in the standard CSI pulse sequence can induce eddy currents, these effects have been observed to have minimal impact on images and are removed from our CSI analysis by subtraction of a reference dataset with no pre-pulse.

2.5. Shielding designs

The shielding for this PET insert consists of two nested cylindrical surfaces connected at each end by a ring extending from the smaller radius cylinder to the larger radius cylinder—making an annular 'can,' see Fig. 1. There are two of these shielding structures, one on either end of the insert, lying on either side of the MRI isocenter. The continuous metal surfaces are capable of supporting undesired eddy currents, most obviously azimuthal eddy currents from the switching of the axial gradient but also more complicated current patterns induced by switching of the transverse gradients. The rollover point for the axial gradient on our system (the point where maximal magnetic field amplitude from the gradient occurs) is located at approximately 7.5 cm axial distance from the isocenter. Our prototype has the shielding located with the inner end of the annular shielding just beyond the rollover point (7.7 cm). However the rollover point is specified on-axis and the shielding is at a fixed radial distance away from the axis where the gradient field is likely to fall off faster with distance from isocenter. Also, at this axial location, field strength from the transverse gradients is likely to be small.

If eddy currents prove to be problematic, alternate shielding designs could be used to reduce the current magnitude. For example, breaks can be cut in the shielding that interrupt the undesired current paths (Alecci and Jezzard, 2002; Hayes and Eash, 1987). To foil azimuthal eddy currents, breaks or slits running along the axial length of the cylinder can be used. Breaks in the shielding can compromise the shielding, but if the only goal is to shield RF noise, then narrow slits will not have much impact (e.g. 1 mm slit compared to 1 m free-space wavelength RF at 300 MHz). Also, two-layer shielding designs could be used with breaks offset from one another (i.e., breaks in one layer being overlapped by solid strips on the other).

3. Methods

3.1. Imaging and image analysis

All MR imaging experiments were performed with a 7 T (300 MHz) Bruker Biospec Magnet with Magnex MKIII gradients (180/120 mm OD/ID). The system console is a Linux based PC running Paravision version 3.0.2. The RF coil is a Bruker 35 mm ID birdcage coil. Before any images were taken, the MRI system was shimmed and tuned with the sample in place in the RF coil. A sequence called Onepulse was used for this purpose with 8192 points and 10 kHz spectral width. Automatic first order and second order shimming macros were used.

Images were acquired with basic gradient echo (GE) sequences (128×128 matrix size, 42×42 mm field of view, 1mm slice thickness, T_R = 500 ms, T_E = 4.1 ms, 8 slices). Receiver gain and digitizer gain settings were the same for all GE acquisitions within each set of experiments. Normalized difference images (with respect to a reference image) were generated by simply performing a pixel-by-pixel subtraction of the image from its reference and then normalizing the result by the reference maximum pixel value. Signal to noise ratio for MRI was calculated

by selecting signal and noise-only regions for magnitude images and accounting for the Rician distribution of noise (Constantinides *et al.*, 1997).

Image errors and distortions were evaluated using image subtraction (subtracting the image from a corresponding reference image). In cases where a single numerical quantification of image error is desired the normalized root mean square error (NRMSE) was used, defined as

$$NRMSE = \sqrt{\frac{1}{N}\sum_i \left(\frac{\alpha \cdot x_i - y_i}{\max(y)}\right)^2}, \quad \text{where } \alpha = \frac{\sum_i x_i \cdot y_i}{\sum_i x_i^2} \tag{1}$$

and where x_i is the intensity of the i^{th} pixel of the image in question (taken at different shielding positions or at different times), y_i is the intensity of the i^{th} pixel of the reference image, and α is a scaling factor (Wolfsberger *et al.*, 2002). The sum is over all N pixels. The fractional difference (or percentage difference if multiplied by 100) relative to the image maximum was produced by dividing by the reference image maximum.

3.2. Baseline measurements

In order to measure baseline error, 13 images of a non-uniform water phantom were taken without moving the phantom or RF coil and with no additional foreign material in the bore. Between images, the autoshim and autotune macros were repeated, but nothing else was changed. NMRSE, Eq. 1, was calculated for each image using the following image as a reference.

3.3. Shielding placement experiments

The copper shielding model used for placement experiments consisted of one (for the asymmetric setup) or two symmetrically placed (for the symmetric setup) cylinders 65 mm in diameter, 115 mm in axial length, and 50.8 μm (0.002”) thick. MR images of a uniform and a non-uniform water phantom were acquired separately for various positions of the shielding model made to slide along the outside of a polycarbonate (Lexan) tube, see Fig. 1, while the RF coil and sample were supported inside the tube. In each experiment, reference images were taken with the shielding outside the MRI bore. Image errors with shielding placed at different locations were quantified by calculating NRMSE, Eq. 1, relative to the reference image taken immediately after each shielding placement. Note that the system was reshimmed and retuned for each new shielding position.

3.4. Chemical shift imaging

In the CSI experiments, a strong gradient pre-pulse was inserted before the regular CSI pulse sequence, see Fig. 2. By changing the delay time (T_d) between the gradient pre-pulse and the start of the standard CSI sequence, we were able to quantify the magnitude of and time-based behavior of the eddy current fields. The gradient pre-pulse was created using the slice select gradient, had an amplitude of 80% of the maximum gradient strength (95 mT/m), and had a duration of 0.01s. Experiments were performed using ten values of T_d: ranging from 0.1 ms to 5 s.

Four different experimental set ups were examined using this CSI analysis: no shielding, 50.8 μm (0.002”) shielding located at d = 5 cm, 76.2 μm (0.003”) shielding at isocenter (d = 0 cm), and the fully constructed PET insert. In each case a uniform phantom filled with ethylene glycol was used. Ethylene glycol has two spectral peaks, a lower magnitude OH peak, and a much higher magnitude CH_2 peak. The CH_2 peak was used in all data analysis because it is insensitive

to temperature fluctuations. The chemical shift of the CH_2 peak was used to assign pixel values. Note that when the PET insert was used, it was physically present but not powered on. For more on simultaneous operation see (Catana *et al.*, 2006).

Standard CSI data were acquired before and after each experiment with the gradient pre-pulse. A representation of the eddy current effects was generated by subtracting the reference field map without the gradient pre-pulse from the immediately preceding data with the gradient pre-pulse. Temporal variation was monitored by comparing the interleaved reference data. Note that the morphological image was acquired with a FLASH pulse sequence. The slice thickness was 1 mm and the field of view was 42×42 mm for the morphological image and all CSI acquisitions. However, the morphological image has a matrix size of 128×128, and CSI has matrix size is 32×32×2048. To further analyze the data, histogram analysis was used. A mask was used to reject the noise-only background pixels from histogram and subtraction analysis.

3.5. Different copper shielding designs

Five different copper shielding models were used to explore the effects of shielding thickness and breaks in the shielding on image error. All five symmetric Cu shields were 65 mm in diameter and 115 mm in axial length. Shielding models A, B, and C were solid copper cylinders made of a single layer with thickness 76.2 μm, 50.8 μm, and 25.4 μm (0.003”, 0.002”, and 0.001”), respectively. Model D is made of a single layer of 50.8 μm (0.002”) copper, but it is cut into 1 cm axial strips with 1 cm gaps between (except at the seam where the pattern wraps around the cylinder). Model E consists of two layers of 25.4 μm (0.001”) copper separated by a layer of standard 20 pound printer paper. The inner layer is solid copper with no breaks, while the outer layer is cut into 1 cm strips spaced by 1 cm.

A symmetric setup was used to perform the shielding placement experiments (Fig. 1) using the polycarbonate support tube to hold the RF coil (inside) and shielding (around the outside). For each shielding model, phantom images were acquired with the axial shielding location, d, ranging from 0 cm to 12 cm in 2 cm increments, and a reference image with the shielding moved out of the bore. GE data was collected (imaging parameters given in Section 3.1) and analyzed by the subtraction method. For each subtraction image, the normalized root mean square error (NRMSE) was calculated (Eq. 1) and plotted.

3.6. PET insert prototype

The prototype PET insert used in this work is based on the use of APDs that are slightly removed from the MRI magnet center and are coupled to lutetium oxyorthosilicate (LSO) scintillator elements with short optical fiber bundles. A detailed description of the PET insert and initial results obtained with the system are published (Catana *et al.*, 2008; Catana *et al.*, 2006). The PET insert is supported by an inner carbon fiber tube. The PET electronics modules are placed at an axial distance of 77 mm from MRI isocenter. The insert shielding (discussed in Section 2.5) is essentially an “annular can” structure surrounding the PET electronics. The inner and outer cylindrical surfaces were each constructed from double-sided flexible copper-clad board (RT/duroid 5870, Rogers Corporation, Connecticut) with a 35 μm thick layer of copper on each side of the substrate and an overall thickness of 0.787 mm (0.031”). The diameters of the inner and outer cylinders are 65 mm and 118 mm, respectively. The axial length of the shielding assembly is 151 mm. During image acquisition, the PET insert electronics are cooled to approximately 4 °C with nitrogen gas in order to reduce the noise and stabilize the system. This PET insert is positioned inside of the gradient coil of the MRI while the RF coil is placed inside of the PET insert. Though this PET insert prototype is built and fully functional, there are still many questions regarding the design that warrant further investigation.

4. Results

4.1. Baseline system variation

Fig. 3a shows the baseline NMRSE as a function of repetition index. Fig. 3b shows the computed normalized SNR (with respect to the SNR of the reference images) and the measured normalized spectral linewidth of the proton NMR signal (with respect to the spectral linewidth of the reference images) for each repetition. The NRMSE variation is clearly not just Gaussian distributed variation about some mean value, however, computing the standard deviation results in 0.005 for GE data. This number is used to generate approximate error bars in subsequent plots to indicate uncertainty.

4.2. Placement of the shielding

The NRMSE measurement with the asymmetric setup and a polycarbonate tube is shown in Fig. 4 (dashed line). The shielding was moved from d = −1 cm (one centimeter past the isocenter) to d = 12 cm in 1 cm increments. A similar plot of NRMSE versus shielding location for the symmetric setup is also shown in Fig. 4 (solid line). Note that reference images taken with the shielding removed from the bore were taken immediately after each shielding location. Error bars are estimates based on baseline NRMSE measurement (see section 4.1). Sample GE images are shown in Fig. 5 for the symmetric shielding example with d = 2 cm and d = 8 cm. Normalized error (difference) images with respect to the reference images are also shown.

4.3. Chemical shift imaging analysis

Chemical shift imaging (CSI) results for the gradient pre-pulse experiment are shown in Fig. 6 for short and long pre-pulse delay times. Fig. 6a is for no shielding. Fig. 6b is a case with 50.8 μm (0.002”) thick shielding placed symmetrically at d = 5 cm. This is similar to the geometry for the shielding in the PET insert. Fig. 6c is for the case with 76.2 μm (0.003”) shielding placed symmetrically at d = 0 cm (close placement and thick shielding should produce larger eddy current related errors). Note that frequency shifts are more prevalent in Fig. 6d, which displays results with the full PET insert prototype in the bore, including electronics and other support and shielding structures that are not part of our simplified shielding model. Histograms of the pixel values (corresponding to chemical shift values in ppm) for these same experiments are shown for more quantitative comparison in Figs. 7 a–d.

4.4. Shielding designs

The NMRSE versus shielding location is plotted in Fig. 8 for five different variations on our simple model for the shielding. For all plots, error bars are estimates based on baseline NRMSE measurement (see section 4.1). Sample GE images for d = 0 cm, where eddy current effects are expected to be largest, are displayed for each of these five shielding models in the top row of Fig. 9 along with the respective normalized error (difference) images.

5. Discussion and Conclusions

All of our experiments confirmed that errors are introduced in MR images when our shielding models were placed near the isocenter of the magnet. However, there were circumstances in which the resulting errors were negligible. First of all, once the shielding or other metal is in place, the system must be carefully reshimmed. For our studies, Bruker’s Onepulse sequence was run with reduced spectral bandwidth and increased acquisition size to adjust first and second order shims manually or with Bruker’s macros. There are, however, many available techniques for achieving good B_0 homogeneity including Fastmap (Gruetter, 1993) and others (Weiger *et al.*, 2006; Koch *et al.*, 2006; Zhao *et al.*, 2005; Hu *et al.*, 1995). Note that all data and images presented were acquired using a standard GE sequence. Duplication of all

experiments using spin-echo (SE) imaging indicated the SE results did not differ substantially enough to warrant inclusion.

Measurements of NMRSE demonstrated that artifacts were indeed introduced by the shielding model and that they became more significant when the shielding was moved closer to the isocenter. Conversely, when the shielding was moved away from the isocenter, the image error was reduced and began to flatten out notably beyond 5–6 cm for our non-uniform phantom. For our uniform phantom, NMRSE was generally smaller and flattened out beyond 2–3 cm. The MRI SNR fluctuated but generally seemed to be independent of shielding location. These numbers validated design parameters for our current prototype with the shielding structure starting at d = 7.7 cm. Thinner shielding material also reduced NRMSE, as did axial cuts in the shielding to interrupt the circumferential eddy current path. Our preliminary exploration of alternate shielding designs indicated locating the PET electronics and shielding closer to the MRI isocenter may be possible with the use of eddy current reducing shielding designs, however further investigation is required. Alternate shielding designs may also be useful at lower field strengths for which the shielding may have to be thicker (see Section 2.1). Note also that the data for shielding model D in particular (with axial gaps preventing azimuthal eddy currents) suggested that eddy currents, not susceptibility artifacts, were likely to be the primary cause of NMRSE measured in these experiments.

It is important to highlight that difference images are deceptively difficult to acquire and interpret for cases where sample position, shims, or other system parameters can change in time. These temporal variations lead to innocuous NMRSE features that can be misinterpreted as errors from some other source or parameter under study (particularly if varied in time). Repeated shimming and scanning resulted in global NMRSE fluctuations on the order of 1–2% of the image max (over 150% in NMRSE value) for a static uniform phantom—local variations were larger, as were global variations for a non-uniform phantom. Despite these uncertainties, the trends noted above were clear and consistent.

Note that the difference images in Fig. 5 and Fig. 9 are dominated by reasonably small edge errors with, for some cases, small and slowly varying deviations in more uniform regions. The edge errors could be a result of differing shim settings between each measurement and the reference or other field effects such as eddy currents. As an aside, we note that these edge errors are the primary reason the NRMSE is larger for the non-uniform phantom. Given the nature of these edge errors, which may not even occur with the full insert in place and with a single set of shim values (recall that error relative to a reference image is a bit of a contrived result —for actual PET/MR imaging a single shim set will be used and motion of sample and RF coil absent in most circumstances), we believe they are not cause for significant concern. If one were planning very precise geometric mapping or measurements, however, we recommend further investigation.

A new technique was developed for studying eddy currents using CSI. This technique confirmed that eddy currents can be induced on our shielding models and that the strength of these eddy currents increased with thicker shielding and with reduced separation of the shielding from isocenter. For short pre-pulse delay times, large shifts of the CH_2 peak were observed (see Fig. 6–Fig. 7)—indicating a large change in local B_0. However, for longer delay times, the shift values were smaller and had an average closer to zero (eddy currents and fields generated by the pre-pulse decay with delay time). The residual effects from the short delay times with no shielding present were an indication of small eddy currents generated on the cryostat of the MR scanner or other metal structures. For Fig. 6d and Fig. 7d, corresponding to the full PET insert in the scanner bore, we observed larger chemical shift values. These results can be directly attributed to increased eddy currents, because the effects of any static field non-uniformities were removed by subtraction of the reference CSI data. Note that the

frequency shift values are larger with the insert in place, despite the fact that the shielding is placed at d = 7.7 cm, because of the presence of the PET electronics and additional shielding structures, including the outer cylinder and annular end rings to the shielding.

The severity of eddy currents using the pre-pulse CSI method are an indication of the relative propensity for the axial gradient (the primary anticipated source of eddy currents because of the shielding geometry and placement) to induce eddy currents for a given arrangement but does not indicate the magnitude of eddy currents induced for any given (standard) imaging experiment. The same CSI method can be used with transverse gradient pre-pulses; this would be particularly important for shielding that extended closer to the axial center of the magnet, where transverse gradient strength is larger. The CSI data confirm that the full PET insert is susceptible to azimuthal eddy currents, but the magnitude of the field or frequency shift is generally less than 0.05 ppm, and we have observed that MR images with the insert in place do not exhibit noticeable artifacts when the system is shimmed and tuned appropriately. Note that induced eddy currents may be different for other imaging sequences or MR systems.

We did not observe any indications that inductive coupling with the shielding or PET insert was causing significant degradation in gradient coil performance for the basic pulse sequences we ran. The fact that eddy currents were observed indicates some coupling is present, however, so this issue should be explored in more depth and corrected for more demanding pulse sequences or other designs and geometries (Duyn *et al.*, 1998).

During related work operating MR and PET systems simultaneously, we have seen no indications that RF noise or RF interference between the two systems is a significant problem for our PET insert design (Catana *et al.*, 2006), though we have observed one potential problem related to RF coupling. While exploring the asymmetric shielding model with one of our two Bruker birdcage RF coils, we experienced a few occasions on which a tight-fitting shielding model (radius only slightly larger than RF coil housing) had significant negative impacts on MR imaging. When the inner axial edge of the shielding model was at approximately the same axial position as the endring of the birdcage coil (approximately d = 3 cm), the coupling between the two structures was enough to detune the RF coil as much as 500 kHz, beyond the programmable range of our system hardware. However, this only occurred for the asymmetric shielding arrangement with small radius shielding and only occurred intermittently (Peng *et al.*, 2006).

For other MR systems or field strengths, results might be different. An insert for 3 T MRI, for example, may require thicker shielding, increasing the likelihood of eddy currents and the possible interest in alternate shielding designs. Also, different gradient geometry and strength could impact the propensity for eddy currents or the gradient waveform fidelity. The techniques detailed in this article provide useful tools for characterizing and quantifying these effects.

In addition to testing design parameters for our PET insert, this work has demonstrated some of the challenges involved in quantifying image errors resulting from foreign objects in the bore of an MR scanner. Comparing two images can be problematic because of changes in system performance, especially due to required re-shimming and re-tuning. If this approach is to be used, variation in system performance should be carefully explored prior to interpretation of results.

We also showed that CSI techniques in general are useful for quantifying the impact of metallic objects on MRI. Most importantly, we demonstrated the use of a novel combination of a 2D CSI experiment with a gradient pre-pulse and variable delay time to explore the extent to which eddy currents can be induced on a foreign object. Standard CSI, on the other hand, can be used to map the field uniformity (i.e. with no pre-pulse or limiting shift behavior for long delay

times) with and without the foreign object present, indicating static B_0 non-uniformities resulting from susceptibility interfaces or other sources.

Acknowledgments

The authors would like to acknowledge and thank Dr. Ciprian Catana and Dr. Yibao Wu for designing and constructing the PET insert, particularly Dr. Catana for his advice and willingness to help throughout the course of this project. We would like to thank the UC Davis NMR Facility for a grant providing development time on the magnet. Thanks also to Dr. Jinyi Qi for invaluable input on numerical quantification of image errors. Support for this project was provided in part by NIBIB Bioengineering Partnership Grant R01 EB000993.

References

Alecci M, Jezzard P. Characterization and reduction of gradient-induced eddy currents in the RF shield of a TEM resonator. Magn Reson Med 2002;48:404–407. [PubMed: 12210952]

Catana C, Procissi D, Wu Y, Judenhofer MS, Qi J, Pichler BJ, Jacobs RE, Cherry SR. Simultaneous in vivo positron emission tomography and magnetic resonance imaging. Proc Natl Acad Sci U S A 2008;105:3705–3710. [PubMed: 18319342]

Catana C, Wu Y, Judenhofer MS, Qi J, Pichler BJ, Cherry SR. Simultaneous acquisition of multislice PET and MR images: initial results with a MR-compatible PET scanner. J Nucl Med 2006;47:1968–1976. [PubMed: 17138739]

Chinzei K, Kikinis R, Jolesz FA. MR Compatibility of Mechatronic Devices: Design Criteria. 1999;2:1020–1031.

Chinzei K, Miller K. Towards MRI guided surgical manipulator. Med Sci Monit 2001;7:153–163. [PubMed: 11208513]

Christensen NL, Hammer BE, Heil BG, Fetterly K. Positron emission tomography within a magnetic field using photomultiplier tubes and lightguides. Physics in Medicine and Biology 1995;40:691–697. [PubMed: 7610123]

Constantinides CD, Atalar E, McVeigh ER. Signal-to-noise measurements in magnitude images from NMR phased arrays. Magn Reson Med 1997;38:852–857. [PubMed: 9358462]

Duyn JH, Yang Y, Frank JA, van der Veen JW. Simple correction method for k-space trajectory deviations in MRI. J Magn Reson 1998;132:150–153. [PubMed: 9615415]

Gaa J, Rummeny EJ, Seemann MD. Whole-body imaging with PET/MRI. European journal of medical research 2004;9:309–312. [PubMed: 15257872]

Giancoli, DG. Physics: principles with application. New Jersey: Prentice Hall; 1995.

Gilbert KM, Handler WB, Scholl TJ, Odegaard JW, Chronik BA. Design of field-cycled magnetic resonance systems for small animal imaging. Phys Med Biol 2006;51:2825–2841. [PubMed: 16723769]

Gruetter R. Automatic, localized in vivo adjustment of all first- and second-order shim coils. Magn Reson Med 1993;29:804–811. [PubMed: 8350724]

Hayes, CE.; Eash, MG. Shield for decoupling RF and gradient coils in an NMR apparatus. US: General Electric Company; 1987.

Hu J, Javaid T, Arias-Mendoza F, Liu Z, McNamara R, Brown TR. A fast, reliable, automatic shimming procedure using 1H chemical-shift-imaging spectroscopy. Journal of magnetic resonance 1995;108:213–219. [PubMed: 7670755]

Jacobs RE, Cherry SR. Complementary emerging techniques: high-resolution PET and MRI. Current Opinion in Neurobiology 2001;11:621–629. [PubMed: 11595498]

Judenhofer MS, Wehrl HF, Newport DF, Catana C, Siegel SB, Becker M, Thielscher A, Kneilling M, Lichy MP, Eichner M, Klingel K, Reischl G, Widmaier S, Rocken M, Nutt RE, Machulla HJ, Uludag K, Cherry SR, Claussen CD, Pichler BJ. Simultaneous PET-MRI: a new approach for functional and morphological imaging. Nat Med 2008;14:459–465. [PubMed: 18376410]

Koch KM, Brown PB, Rothman DL, de Graaf RA. Sample-specific diamagnetic and paramagnetic passive shimming. Journal of magnetic resonance 2006;182:66–74. [PubMed: 16814580]

Lewellen TK. Recent developments in PET detector technology. Phys Med Biol 2008;53:R287–R317. [PubMed: 18695301]

Lucas AJ, Hawkes RC, Ansorge RE, Williams GB, Nutt RE, Clark JC, Fryer TD, Carpenter TA. Development of a combined microPET-MR system. Technol Cancer Res Treat 2006;5:337–341. [PubMed: 16866564]

Peng, BJ.; Catana, C.; Walton, JH.; Cherry, SR.; Willig-Onwuachi, J. Proc. Intl. Soc. Mag. Reson. Med. Seattle, Washington, USA: 2006. Placing a PET insert in the bore of a 7T magnet: Initial study of the interactions of the MRI system with the PET shielding.

Rumpel H, Pope JM. Chemical shift imaging in nuclear magnetic resonance: A comparison of methods. Concepts in Magnetic Resonance 1993;5:43–55.

Shao Y, Cherry SR, Farahani K, Meadors K, Siegel S, Silverman RW, Marsden PK. Simultaneous PET and MR imaging. Phys Med Biol 1997;42:1965–1970. [PubMed: 9364592]

Shen, L.; Kong, JA. Applied electromagnetism. Boston: PWS Publishing Company; 1995.

Slates RB, Farahani K, Shao Y, Marsden PK, Taylor J, Summers PE, Williams S, Beech J, Cherry SR. A study of artefacts in simultaneous PET and MR imaging using a prototype MR compatible PET scanner. Phys Med Biol 1999;44:2015–2027. [PubMed: 10473211]

Tidwell AS, Jones JC. Advanced imaging concepts: A pictorial glossary of CT and MRI technology. Clinical Techniques in Small Animal Practice 1999;14:65–111. [PubMed: 10361360]

Townsend DW. Multimodality imaging of structure and function. Phys Med Biol 2008;53:R1–R39. [PubMed: 18263942]

Tse ZT, Janssen H, Hamed A, Ristic M, Young I, Lamperth M. Magnetic resonance elastography hardware design: a survey. Proc Inst Mech Eng H 2009;223:497–514. [PubMed: 19499839]

Ulaby, FT. Fundamentals of applied electromagnetics. Upper Saddle River: Prentice-Hall, Inc.; 2001.

Weiger M, Speck T, Fey M. Gradient shimming with spectrum optimisation. Journal of magnetic resonance 2006;182:38–48. [PubMed: 16807016]

Wolfsberger S, Rossler K, Regatschnig R, Ungersbock K. Anatomical landmarks for image registration in frameless stereotactic neuronavigation. Neurosurgical review 2002;25:68–72. [PubMed: 11954768]

Zaidi H, Mawlawi O, Orton CG. Point/counterpoint. Simultaneous PET/MR will replace PET/CT as the molecular multimodality imaging platform of choice. Med Phys 2007;34:1525–1528. [PubMed: 17555233]

Zhao YS, Anderson AW, Gore JC. Computer simulation studies of the effects of dynamic shimming on susceptibility artifacts in EPI at high field. Journal of magnetic resonance 2005;173:10–22. [PubMed: 15705507]

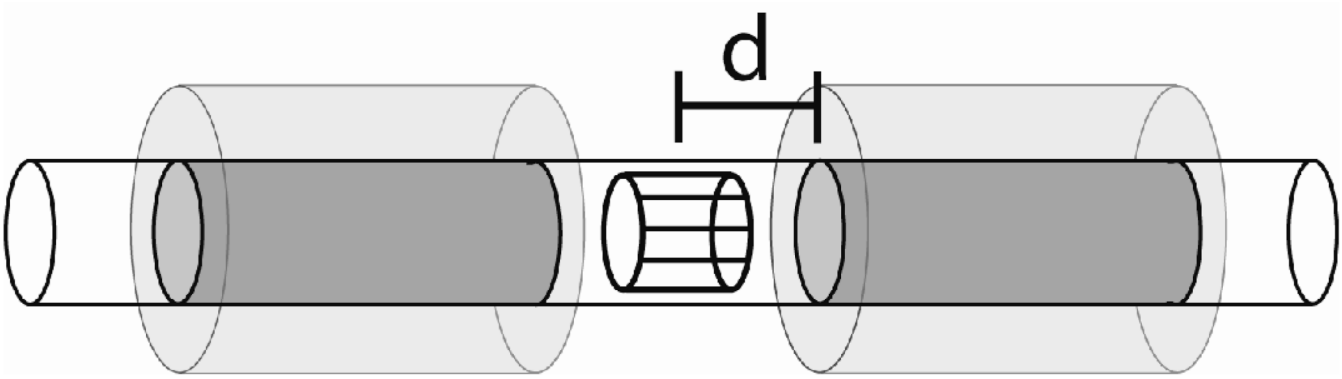

Figure 1.

Diagram of the shielding geometry (not to scale). The long clear cylinder represented the plastic support tube used for shielding placement experiements. The dark shaded cylinders represent the copper shielding used for out symmetric shielding model placed at a variable axial distance 'd' from the magnet isocenter. (The asymmetric shielding experiments used only, i.e., the right shielding cylinder.) The RF coil is shown inside the plastic tube surrounding the imaging volume at the center. The lightly shaded regions indicates the volume in which the PET electronics and outer shielding is located for the full PET insert. Note that this whole structure is placed inside the MR scanner.

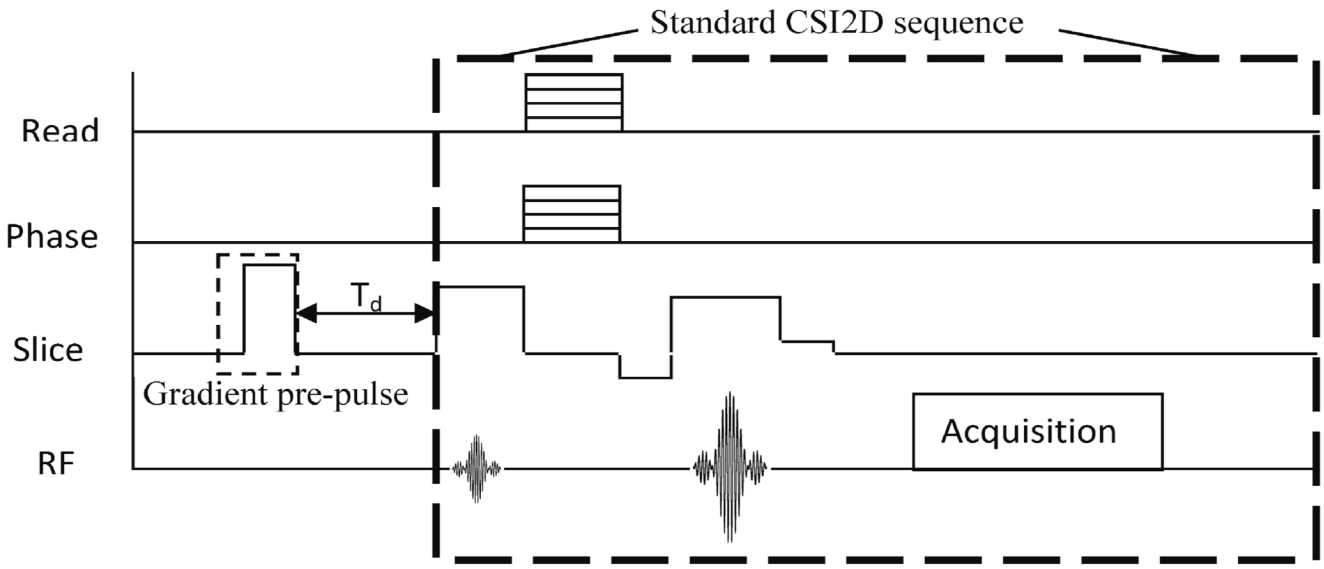

Figure 2.
A simple pulse sequence diagram illustrates the modified CSI2D experiment with a gradient pre-pulse inserted in the slice select direction. T_d, the time from the pre-pulse to the start of the standard CSI2D sequence was varied.

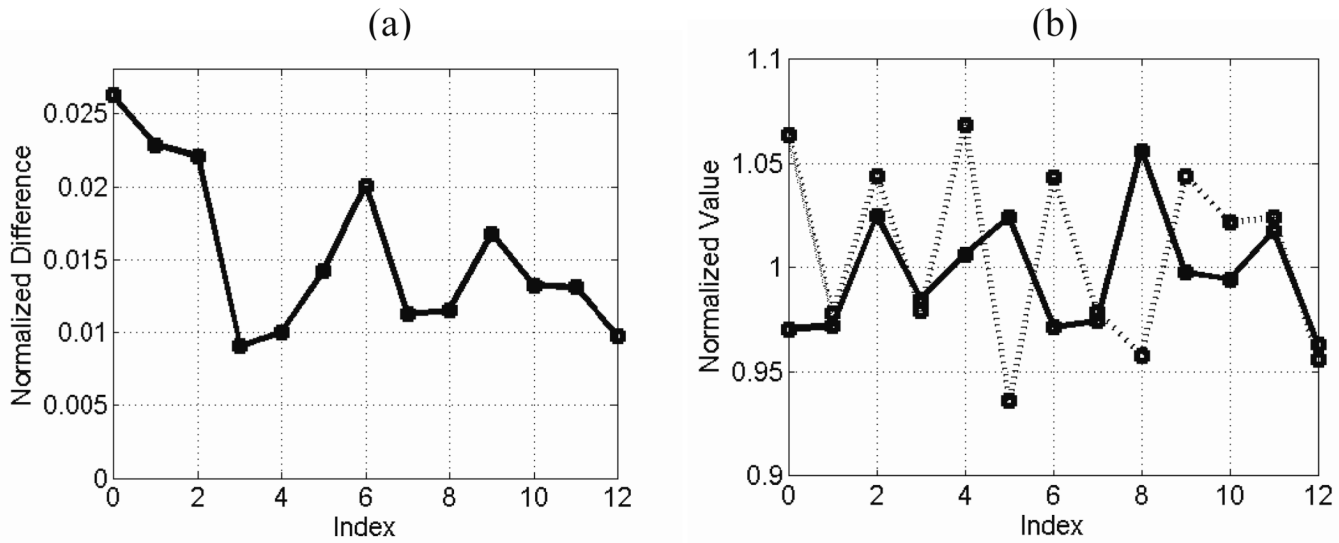

Figure 3.

Baseline error measurement: repeated images were taken of a non-uniform water phantom (reshimming each time) without any shield or tubes present and were analyzed for baseline variation. Plots are shown of (a) NMRSE, (b) normalized SNR (solid line), and normalized linewidth (dashed line) versus repetition index.

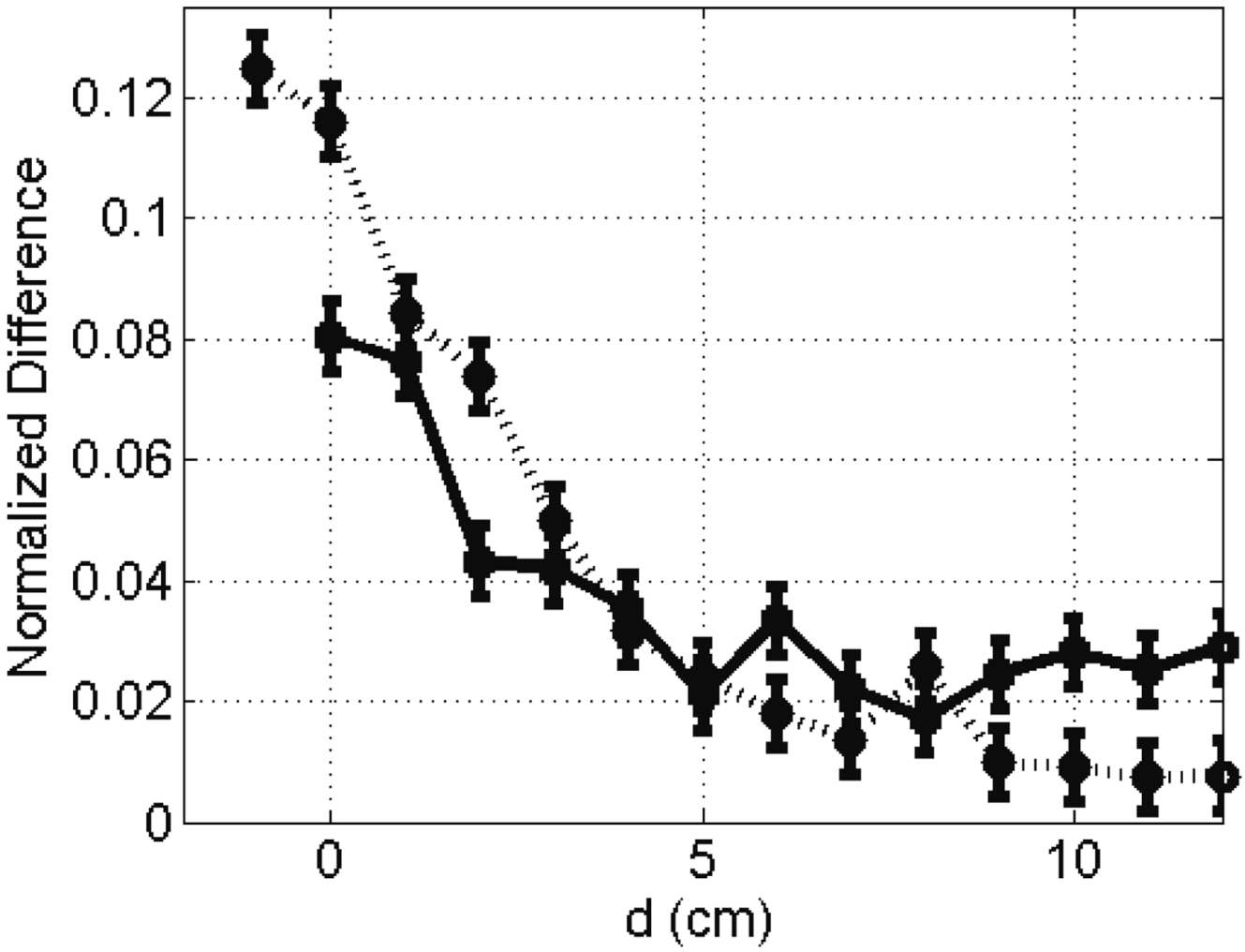

Figure 4.
Shielding placement experiment: NMRSE versus shielding location (d) is plotted for the symmetric (solid line) and asymmetric (dashed line) shielding models. Error bars are added to give an approximate indication of baseline variation.

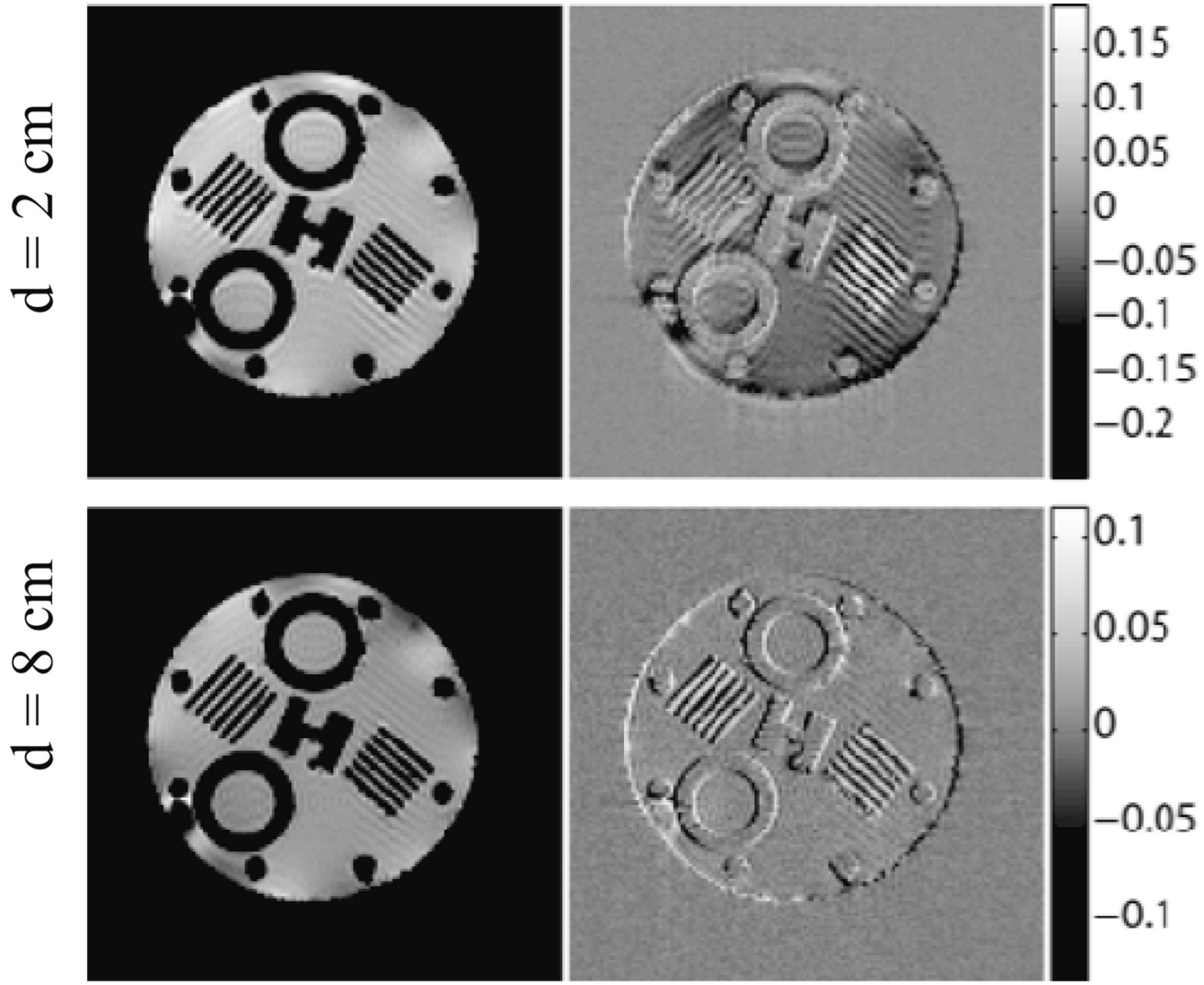

Figure 5.
GE images are displayed for shielding locations d = 2 cm (top) and d = 8 cm (bottom) using the shielding model. Normalized error (or difference) images with respect to the reference images are shown to the right of each GE image with color bars of error values normalized to reference image maxima.

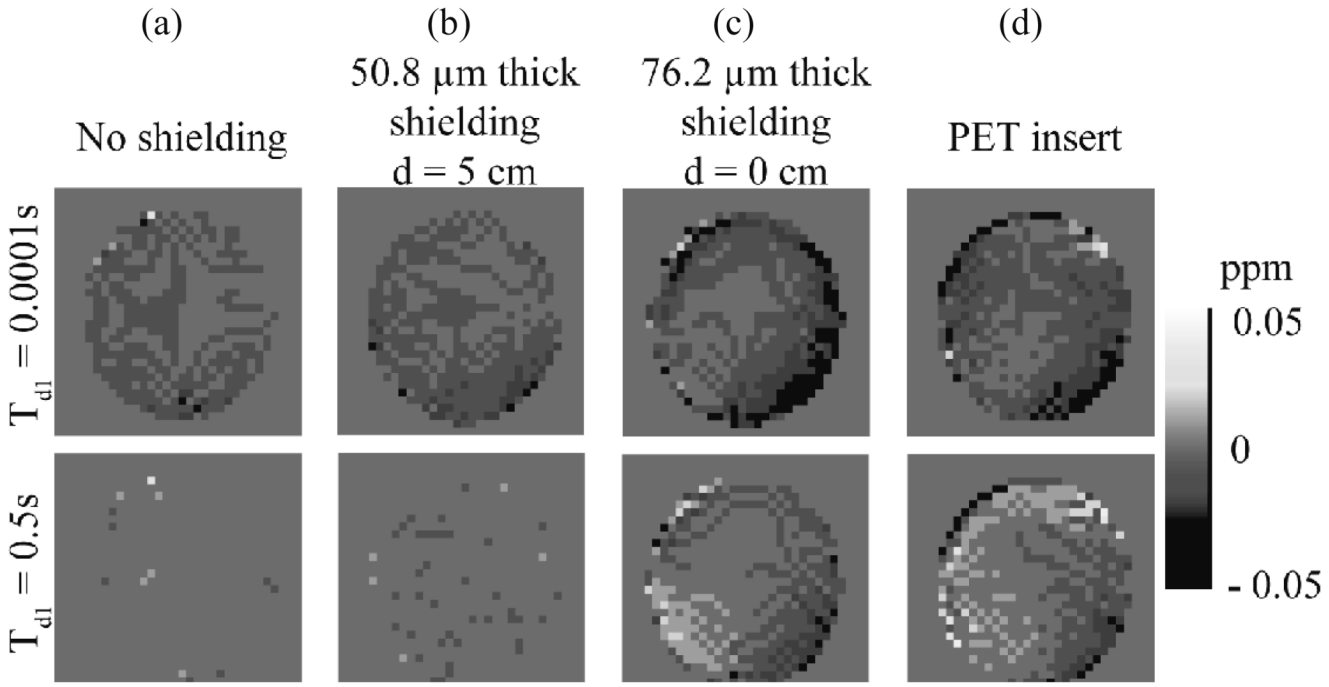

Figure 6.

CSI data give visual representations of induced eddy current fields. These images show maps of the pixel-by-pixel shift in resonance frequency (for CH_2) resulting from the gradient pre-pulse (shift from frequency with no pre-pulse). Two different pre-pulse delay times are shown (top row 0.0001 s, bottom row 0.5 s) for four different cases: (a) no shielding present, (b) 50.8 μm (0.002”) symmetric shielding model placed 5 cm from iso-center, (c) 76.2 μm (0.003”) symmetric shielding model placed at iso-center, and (d) the actual PET insert. The color bar at the right indicates the magnitude of the frequency shift in ppm.

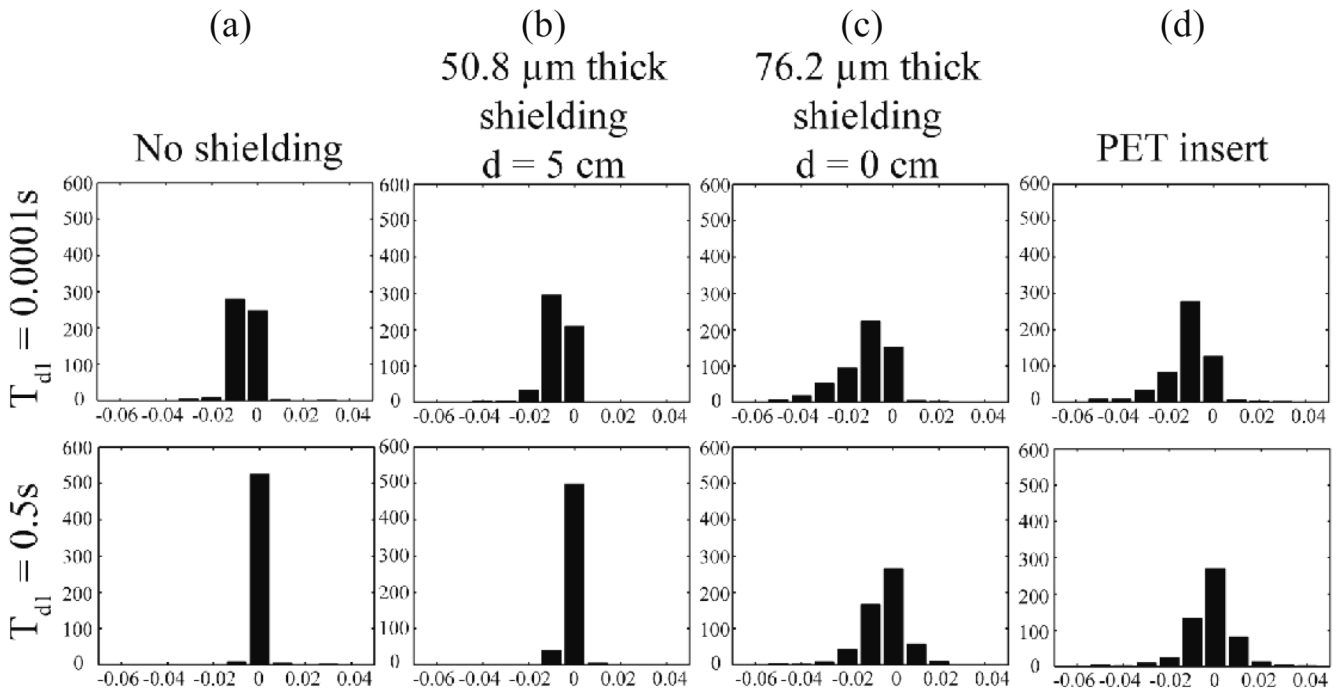

Figure 7.

Histograms are plotted of the frequency shifts shown in Fig. 6. Results are shown for (a) no shielding, (b) 50.8 µm (0.002”) shielding model at d = 5 cm, (c) 76.2 µm (0.003”) shielding model at d = 0 cm, and (d) the full PET insert. Top (bottom) row corresponds to T_d = 0.0001 s (0.5 s).

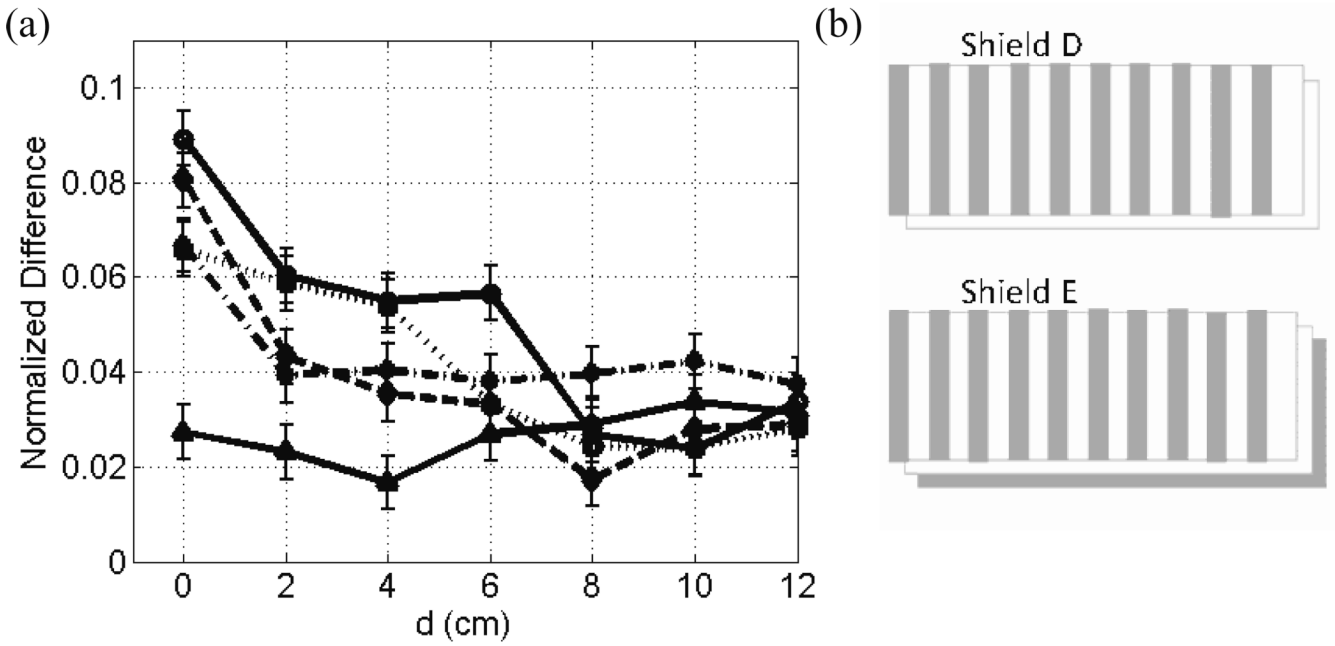

Figure 8.

Plots comparing NMRSE for alterations in the shielding model are shown. NMRSE data versus field location are plotted for five different shields. Shield A (solid line with circles), B (dashed line), and C (dotted line) are continuous copper cylinders of a single layer with a thickness of 76.2 μm, 50.8 μm, and 25.4 μm (0.003”, 0.002”, and 0.001”) respectively. Shield D (solid line with triangles) is 50.8 μm (0.002”) thick with axial gaps. Shield E (dash-dotted line) has two 25.4 μm (0.001”) layers such that the outer one has axial gaps and the inner one is solid. Diagrams of shields D and E are shown unwrapped in (b).

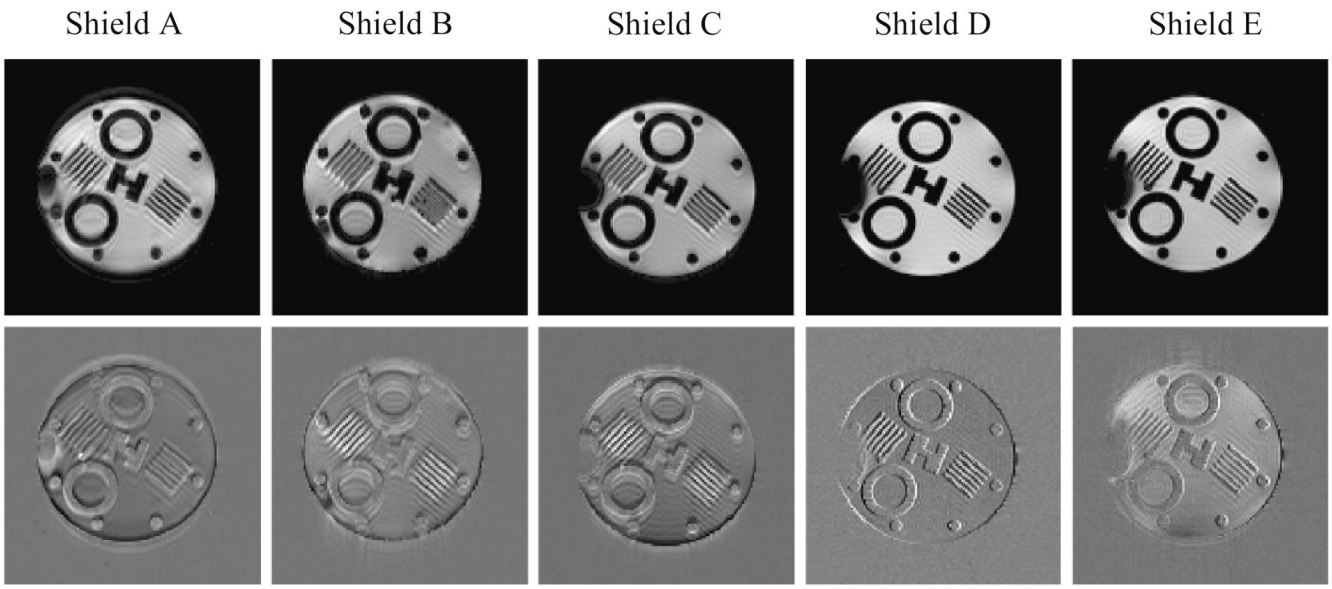

Figure 9.

GE images (top row) are shown for five different shielding models. All images were acquired with d = 0 cm. Corresponding normalized error (difference) images, with respect to reference images, are shown in the bottom row. Shields A, B, and C are continuous copper cylinders of a single layer with thickness of 76.2 μm, 50.8 μm, and 25.4 μm (0.003”, 0.002”, and 0.001”) respectively. Shield D is 50.8 μm (0.002”) thick with axial gaps. Shield E has two 25.4 μm (0.001”) thick layers—the outer one with axial gaps.